Restoration of Authentic Position of Unidentified Vessels in SAR Imagery: A Deep Learning Based Approach

Juyoung Song, Duk-jin Kim 🅾, *Senior Member, IEEE*, Sangho An, and Junwoo Kim

Abstract—Enhancement of vessel detection performance in synthetic aperture radar (SAR) images generated academic advancements related to amelioration of the algorithmic accuracy and training data procurement. For practical implementation of vessel detection algorithm to maritime surveillance, however, presentation of authentic position of vessels was essential. Accordingly, this article aimed to propose an algorithm, which demonstrated realistic and azimuth shift-corrected position of vessel, especially out of conventional vessel monitoring apparatus: automated identification system (AIS) and vessel-pass (VPASS) information. Two different analyses regarding the vessel detection output utilization were, therefore, presented. Primary analysis demonstrated a vessel identification algorithm, comparing the vessel detection output with elaborately preprocessed AIS and VPASS information, which indicated the discrete position and velocity of vessel. The other presented a position restoration algorithm via i) velocity estimator complementing the conventional fractional Fourier transform velocity estimation analysis, while investigating the effect of range acceleration in deriving the azimuth velocity and ii) measuring the vessel orientation angle from Radon transform. Both algorithms were implemented to the vessel detection output in Cosmo-SkyMed SAR images, depicting an enhanced accuracy compared to the conventional algorithm both in velocity estimation and azimuth shift estimation; velocity offset reduced from 1.64 m/s to 1.29 m/s and average azimuth shift offset reduced from 70.75 m to 62.39 m. The presented algorithms would be decisive in terms of practicality if robustly attached to convolutional neural network-based vessel detection algorithms demonstrating ideal detection performances.

Index Terms—Automated identification system (AIS), azimuth shift, fractional Fourier transform (FrFT), vessel identification, and vessel-pass (VPASS).

I. INTRODUCTION

MONITORING vessels in littoral and oceanic regions was essential due to their roles in navy and fishery [1]. A number of academic attempts were made to augment the monitoring

efficiency and accuracy, most of which focusing on detection [2]–[5]. Vessel detection has been widely conducted in synthetic aperture radar (SAR) imagery, which provides the weather independent detection platform [6]. As the necessity of vessel detection increased especially under inhospitable condition such as stormy seas, sunlight shortage, and inaccessible region of interest, SAR image-based vessel detection demonstrated its superiority over detection in other remote sensing platforms in terms of robust application [7].

The implementation of machine learning algorithm to vessel detection in SAR imagery was prevalent after its introduction, especially the convolutional neural network (CNN) for image processing [8]–[11]. Unlike the previous detection algorithms such as the constant false alarm rate and threshold-based measurements, which focused on the brightest points of the image section, CNN-based detectors distinguished the pattern of the vessel inside the SAR image, of which the internal structures and reflection were characterized and limited [12]. Machine learning, especially when using CNN-based detectors, often outperformed traditional detectors in both accuracy and efficiency in diverse SAR data acquisition conditions [13].

As the predominant objective of vessel detection was considered as performance enhancement, a number of previous studies regarding it focused on the amelioration of CNN-based detection algorithm architecture. Comparison between two or more conventional algorithms were often conducted, driving the most accurate algorithm between them, such as regions with CNN(R-CNN) [14], fast R-CNN, faster R-CNN [15], and you only look once (YOLO) [16]. Variations of the CNN-based detectors were also tested against one another: HSV-YOLO (H-YOLO) [17], hierarchical CNN [18] and Grid-CNN [19]. Nearly what all of these algorithmic studies had in common was performance enhancement, instead of its practical application on vessel monitoring. A deviation from this article stream included the robust construction of training database for vessel detection, as the CNN-based vessel detection demanded both of the detector and training dataset. A database containing vessel chips from the SAR image was presented as OpenSARShip [20] by preprocessing information from vessel including discrete position and velocity: automated identification system (AIS). Enhancement and intensification of vessel training database construction algorithm were additionally presented, implementing a robust interpolation and preprocessing of AIS information [21].

AIS information including position and velocity of each vessel in discrete and irregular manner was regarded as a conventional apparatus of vessel surveillance, but its latest application includes combined research with remotely sensed data such as SAR [22] and electro-optical (EO) satellite images [23]. As the majority of AIS information was not acquired in the desired SAR acquisition time, a number of interpolation procedures were presented to estimate precise and accurate AIS information, which corresponds to the SAR and EO images: linear interpolation, circular interpolation [24], and Kalman filter [25]. From these studies conducted, high detection performance and robust operation of SAR image-based vessel detector via training database were anticipated. Nevertheless, the detected vessels from CNN-based object detector were yet to imply any additional information besides the position of target in the corresponding SAR image.

Conventional studies additionally focused on the acquisition of information in the SAR image containing the target. One of the felicitous examples of extracting information from SAR images was moving target indication (MTI). MTI discerns the maneuvering target from its background, given that the target signal was demonstrated differently in two or more receiving antennas [26]–[29]. It was able to be implemented either from the subtraction of amplitude images or from the interference of phase images, respectively, designated as displaced-phase-center antenna (DPCA) [30], [31] and along-track interferometry (ATI) [32], [33]. Nevertheless, MTI demands SAR images with multiple receiving channels to be implemented, which hinders the application towards single-channeled SAR images. Due to such restriction, majority of studies regarding the velocity measurement via satellite SAR MTI were implemented to TerraSAR-X and TanDEM-X data [34], [35].

Under conditions where MTI were inapplicable, velocity estimation of moving target could be regarded as an alternative. This procedure was often consecutively conducted with generation of sublook images from single look complex (SLC), as a part of multilooking procedure [36]. As the velocity and acceleration of moving target defined the Doppler frequency, the movement of the target was able to be restored by analyzing the difference and offset between the sublook images: images generated from severed Doppler spectrum [37], [38]. Various studies succeeded to implement the velocity measurement without rendering sublook images by directly measuring the azimuth frequency modulated (FM) rate; one of the studies restored the azimuth velocity term while surmising the effect of acceleration on velocity measurement separately [36], the other ameliorated the algorithm to the extent where it could be applied to airborne ATI [39], [40]. Both analyses implemented fractional Fourier transform (FrFT), a generalized conformation of conventional Fourier transform conducted with respect to a given angle [41].

For the associated application of AIS information and remote sensing platforms, matching the detection output with preprocessed AIS information was implemented [22]. The comparison between SAR image-based detection and AIS information derived the vessel identification [42]; speculating its potential hazard from AIS-deprived detection output while assuming the AIS specifications of vessel from precisely matched detection.

In case, where the position sensor was not deployed could be regarded as an intimidation to marine safety and security, such as illegal fishing vessel or martial intrusion. Practical and accurate surveillance on those vessels, therefore, would be a fundamental intention of vessel detection and monitoring.

A number of studies regarding the vessel monitoring on SAR image platform targeted the enhancement of detection performance. The detection outputs, however, were influenced by azimuth shift, physical azimuthwise offset imprinted to target loci in the SAR image caused by radial velocity of the moving target [22]. This shift ought to be calibrated in order to demonstrate the authentic position of the vessel detected and additionally implemented to practical monitoring and surveillance of vessels. Such algorithm would be applicable when vessel monitoring apparatus, such as AIS, are unavailable. This article aimed to discern the detected vessels without monitoring apparatus and then replace the detected position to authentic position of vessel by estimating its velocity and maneuvering angle. Accordingly, three methodologies were presented and assessed as follows:

1) vessel identification algorithm based on conventional vessel surveillance information;
2) velocity estimator implementing FrFT on vessel signal in the SLC images; and
3) measuring maneuvering orientation of vessel via Radon transform and deriving the quantity of azimuth shift from the materials acquired.

The rest of this article is organized as follows. In Section II, the datasets implemented to demonstrate the proposed analyses are briefly introduced, including the input SAR images, AIS and Vessel-pass (VPASS) information, along with the preprocessing procedure of those datasets before implemented to the following section. In Section III, detection, identification, and position restoration of vessel detection output are presented. In Section IV, the results of applying the methodologies of Section III are demonstrated and accordingly analyzed and evaluated with respect to previous studies in Section V. Finally, Section VI concludes this article.

II. DATA ACQUISITION

A. Input Data Acquisition

Vessel detection was performed in SAR images after being trained using the identical form of SAR images, which indicated that the SAR images for training and testing shared the identical arrangement, but completely separated from each other. SAR images for this analyses included Cosmo-SkyMed Stripmap mode Himage in SLC. 16 SLC images as in Table I were acquired in the vicinity of South Korean littoral region in order to associate with vessel position information below and to contain several vessels near harbors of South Korea.

Information from vessels discretely obtained indicating their position and location was often demonstrated as AIS information [20]–[23]. Small fishing vessels to which AIS sensors were not attached, VPASS sensor was operated as a supplementary sensor. VPASS is analogous to AIS system, which transmits the location and velocity of fishing vessel in a discrete manner [43]. Unlike the AIS sensor often attached to vessels regardless of their usages

TABLE I
Cosmo-SkyMed SAR Satellite Images for Vessel Detection

Path	Mode	Acquisition time(UTC)	Average Latitude [N°]	Average Longitude [E°]	Usage
Descending	Himage	04/03/2018 09:16:13~09:16:19	36.0394	129.4475	Test
Descending	Himage	22/07/2018 09:16:29~09:16:35	36.0387	129.4554	Test
Descending	Himage	14/10/2018 09:16:36~09:16:43	36.0371	129.4465	Test
Descending	Himage	19/02/2019 09:16:36~09:16:43	36.0344	129.4578	Training
Descending	Himage	08/04/2019 09:16:40~09:16:46	36.0405	129.4465	Training
Descending	Himage	01/10/2019 09:16:53~09:17:00	36.0369	129.4453	Training
Descending	Himage	05/03/2019 09:29:04~09:29:11	34.8121	126.5004	Training
Ascending	Himage	10/03/2018 21:07:50~21:07:57	34.7286	127.7444	Training
Ascending	Himage	08/07/2018 21:08:08~21:08:15	34.7317	127.7455	Training
Ascending	Himage	13/05/2018 21:07:59~21:08:06	34.7313	127.7440	Training
Ascending	Himage	13/03/2019 21:08:11~21:08:19	34.7362	127.7570	Training
Ascending	Himage	16/05/2019 21:08:20~21:08:27	34.7297	127.7469	Training
Ascending	Himage	09/01/2019 21:07:42~21:07:49	34.7262	127.7605	Training
Ascending	Himage	09/11/2018 21:08:15~21:08:23	34.7307	127.7454	Training
Ascending	Himage	12/01/2019 21:08:12~21:08:20	34.7291	127.7516	Training
Ascending	Himage	06/09/2018 21:08:08~21:08:15	34.7250	127.7533	Training

and magnitudes, the establishment of VPASS sensor on vessels was restricted to small-scale fishing vessels. The implementation of both AIS and VPASS information was expected to affiliate majority of vessel in the corresponding SAR image, which could improve the accuracy and reliability of vessel identification procedure presented in the following section.

Both AIS and VPASS data were consisted of dynamic and static information; dynamic information describes the discretely obtained information, which is renovated as the vessel maneuvers, while static information dictates the detailed specification of vessels left unchanged as the vessel operated. As the vessel maneuvers and dynamic information is rehabilitated, an additional row is concatenated to dynamic information of a previous stage including the acquisition time of the specific row, position of sensor as latitude and longitude, velocity, and vessel identification number. The velocity is presented as course-over-ground (COG) and speed-over-ground (SOG), demonstrating the maneuvering angle with respect to the North Pole and the speed in knot dimension towards it, respectively [44]–[46]. Static AIS information contained the vessel identification number, type of the vessel and dimension indicating the exact allocation of AIS sensor inside each vessel; static VPASS information presents the length and beam of each vessel instead of the complete dimension. Both AIS and VPASS information was acquired for 10 min span, including the SAR acquisition time between it.

B. Input Data Preprocessing

The SAR images were preprocessed through radiometric and geometric calibration. Training and detection of CNN-based vessel detector were conducted on the preprocessed SAR image data with 3 m of spatial resolution. Both the SLC images (L1A) and the images after radiometric and geometric calibration (L1C) were employed for further analyses in Section III.

AIS and VPASS information corresponding to the SAR image dataset ought to be preprocessed accurately in order to be implemented. The preprocessing operation introduced in this article focused on the affiliation of discrete AIS and VPASS information with the vessel signatures in the SAR images.

As dynamic AIS and VPASS information was obtained in discrete manner, all information was interpolated with respect to the mean acquisition time. This clearly leaves interpolation offset, especially for vessels in the edge of the SAR image. Therefore, for each interpolated position of vessels, SAR acquisition time was referred to and again interpolated with respect to it. The procedure was repeatedly implemented until the interpolation failed to exceed the spatial resolution of the SAR image. In such circumstances, all vessels operating with AIS or VPASS information was able to be interpolated abiding by the respective target interpolation time. The Kalman filter was introduced to the interpolated position and velocity to eradicate the intrinsic device error from the AIS and VPASS sensors. The form of Kalman filter followed that of [25].

Maneuvering target in SAR images generated a modification in slant range, demonstrated as a defocusing in azimuth compression and physical azimuth shift imprinted in the SAR image. The approximated equation indicating the difference in slant range via velocity and acceleration of maneuvering target was denoted in (1), where the exact quantity of azimuth shift was demonstrated in (2), derived by the linear term of (1) [39], [47]

$$R(\eta) = R_0 + \frac{y_0 v_{y_0}}{R_0}\eta + \frac{1}{2R_0}((v_a - v_{x_0})^2$$
$$+ v_{y_0}{}^2 \left(1 - \left(\frac{y_0}{R_0}\right)^2\right) + y_0 a_{y_0})\eta^2 \qquad (1)$$

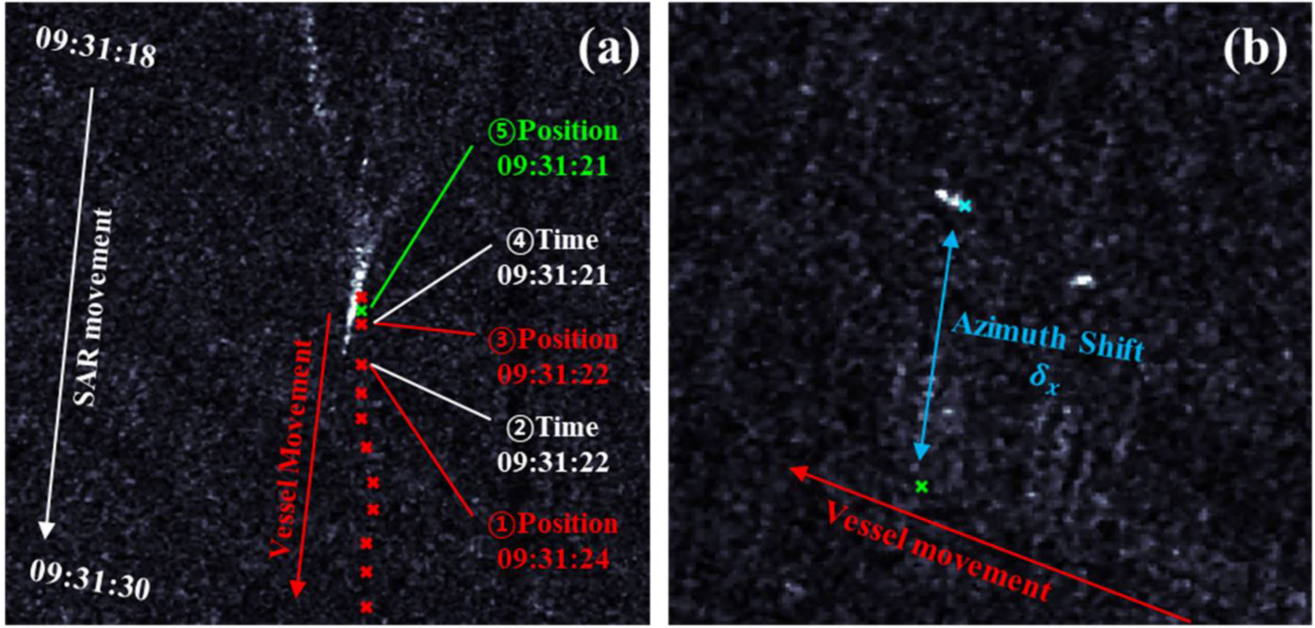$$\delta_x = \frac{R_0}{v_a} v_{y_0}. \qquad (2)$$

Fig. 1. Schematic expression of AIS and VPASS information preprocessing. (a) Interpolation by measuring different target interpolation time in the SAR image. (b) Correction of azimuth shift caused by the vessel movement. The color red, white, green, and blue, respectively, represents AIS information, SAR image acquisition time, vessel position after interpolation, and procedure of azimuth shift correction.

$R(\eta)$ and R_0 denotes the slant range for moving target in slow time η and boresight, respectively, where notation *x, y, v,* and *a* stands for the azimuth, range direction, velocity, and acceleration, respectively. SAR platform velocity and target range velocity are noted as v_a and v_{y_0}, while azimuth shift marked as δ_x.

In order to remove the azimuth shift and match AIS and VPASS information in accurate position of the corresponding SAR image, shift from (2) was compensated by measuring the factors composing it. Target range velocity was estimated by (3), where θ_h indicates platform heading angle and SOG, COG denotes the interpolated SOG and COG

$$v_{y_0} = \text{SOG}\sin\left(\text{COG} - \theta_h\right). \quad (3)$$

Restoration of elliptic satellite path was deliberated for precise measurement of the slant range and satellite velocity for target AIS or VPASS information [48]. For celestial bodies, their elliptic paths were elaborated by six parameters, defined as orbital elements or Kepler parameters; these elements are comprised of eccentricity, semimajor axis, inclination, the longitude of ascending node, the argument of periapsis, and true anomaly. As ancillary data for each SAR image included the data for regularly obtained state vector, geocentric position, and velocity of platform, it was able to generate a set of orbital elements for each row of state vector. In order to restore the average satellite passage, each consisting element was averaged. The output averaged single set of orbital elements indicated the average movement of the platform. From such course, position and velocity of the platform corresponding to time-interpolated AIS and VPASS information was driven for every pulse repetition interval, which was decisive in estimating the platform velocity and slant range. Azimuth shift correction was then terminated after deriving the

quantity of δ_x from (2) and indicating it to interpolated AIS and VPASS information. AIS and VPASS information after being transformed via interpolation and azimuth shift correction was regarded to represent the corresponding position of the target vessel in the SAR image.

Fig. 1 illustrates the two procedures consisting the preprocessing of dynamic AIS and VPASS information. Completing the procedures of interpolation and azimuth shift correction, dynamic AIS, and VPASS information was assigned to the desired location of corresponding vessel in the SAR image. Preprocessed information of AIS and VPASS was implemented to identification of vessels in Section III, as a reference indicating the authentic location of the detected vessels.

III. METHODOLOGY

The analyses regarding the detection, identification, and restoration of authentic position via estimating velocity and orientation of vessel were presented in this section. An introduction to CNN-based object detection algorithm and the corresponding superposition with preprocessed AIS and VPASS information was elaborated first, followed by the estimation of velocity and maneuvering direction of the vessels implementing an enhanced FrFT-based velocity estimator and Radon transform. Fig. 2 describes the entire procedure of detection, identification, and position restoration by means of a flowchart.

A. Detection and Identification of Vessels

Prior to the procedures of identification and velocity estimation, vessel detection output ought to be derived from the SAR images. The vessel training data acquisition algorithm was previously presented, matching discrete information from the
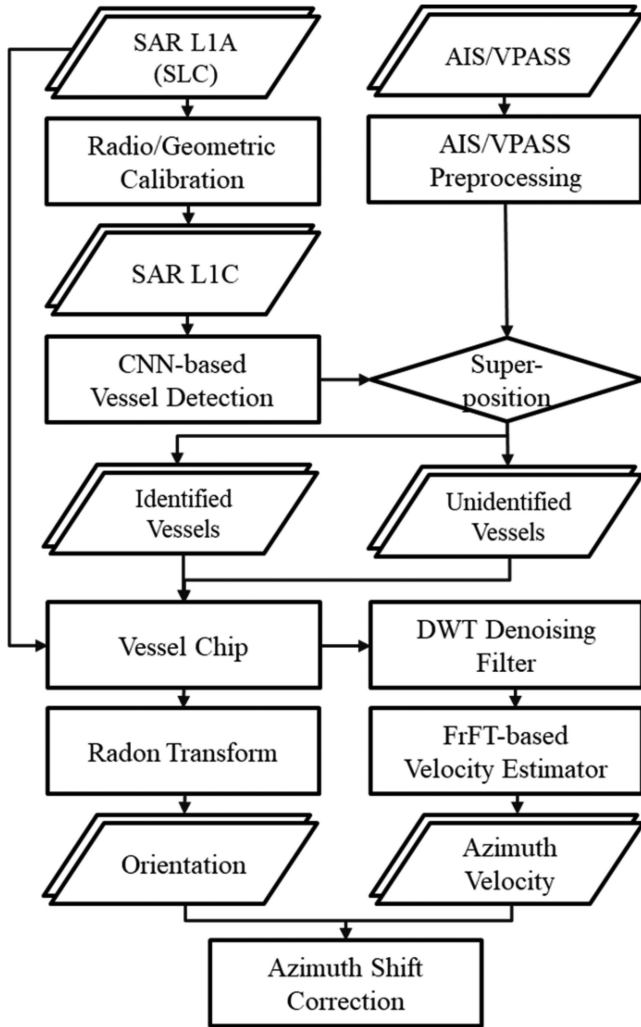
Fig. 2. Flowchart indicating the analyses on vessel identification and authentic vessel position restoration by calibrating azimuth shift.

TABLE II
VESSEL DETECTION PERFORMANCE ON COSMO-SKYMED SAR IMAGES

Acquisition Date	Precision [%]	Recall [%]	F1 [%]
Overall	**89.55**	**57.38**	**69.92**
04/03/2018	88.46	58.97	70.76
22/07/2018	92.68	56.72	70.37
14/10/2018	87.50	56.45	68.63

information of probable vessels instead of authentic vessels, since a detector demonstrating absolute and impeccable accuracy was practically impossible to be generated. The ensuing analyses, however, are intended to be implemented to vessel detection output instead of false alarms. The indicators assessing the accuracy of detector were often elaborated by precision and recall as (4) and (5), respectively; precision was defined as a ratio of the number of accurately detected targets (N_a) and the number of total detection (N_d), where recall was defined as the number of accurately detected targets divided by the number of targets in the detection field (N_t) [18]. However, as precision and recall is under compromising relationship between each other, the harmonic average of precision and recall, entitled as F1 score in (6), was widely implemented as a general performance indicator

$$Pr = \frac{N_a}{N_d} \tag{4}$$

$$Re = \frac{N_a}{N_t} \tag{5}$$

$$F1 = \frac{2PrRe}{Pr + Re} . \tag{6}$$

Therefore, among a number of detection experiments, the model demonstrating high precision instead of recall was preferred in order to minimize false alarm regarded as vessels in further analyses. The assessment of vessel, which was regarded as properly detected was conducted by implementing Intersection over Union (IoU), defined as an area of intersection (A_i) divided by that of union (A_u) between two different rectangles as in (7) and [18]. Abiding by the condition of detection in SAR images containing a number of small vessels, which induced the IoU plunge drastically accompanied by a trivial offset of bounding box, the threshold of IoU determining the detection was configured as 0.2

$$IoU = \frac{A_i}{A_u} . \tag{7}$$

The selected detection output and its performance were denoted in Table II. The algorithm derived much higher precision than in recall. The ensuing analyses were conducted on the output of the algorithm as presented in Table II.

The analysis on unidentified vessel confirmation was conducted by superposing the detection output of vessels over preprocessed AIS and VPASS information completed in Section II. It implies that AIS and VPASS information ought

vessel to the corresponding SAR image. Unlike the procedure of training data acquisition in [21], which was implemented to AIS information, training data for this article was generated from both AIS and VPASS information.

The SAR images after radiometric and geometric calibration illustrated as training data in Table I and corresponding training data of vessels were given as an input to the object detector. Among handful of CNN-based object detectors, an algorithm regarded as up-to-date, of which the performance was continuously enhanced and demonstrated high accuracy in general field of object detection was selected: YOLO version 4 (YOLOv4) [49]. YOLO had been repeatedly advanced after its first presentation, which was praised for its several advantages: i) fast operation, ii) simple and straightforward algorithm, and iii) one-way analysis of training data without implementing a separate extractor [50].

As denoted in Table I, from 13 Cosmo-SkyMed SAR images containing 4538 vessel training data, YOLOv4 object detector was trained and then tested to 3 Cosmo-SkyMed SAR images with 207 vessels. The detection output of vessel includes

to be in an identical format with the detection output: rectangle-shaped bounding box. Static AIS and VPASS information was implemented in order to define the size, width, and height, of AIS/VPASS-based bounding boxes. In case of AIS information, summation of Dimension A and B corresponds to the length of vessel, where summation of Dimension C and D corresponds to the beam of vessel. The reference boxes for identification were created with respect to the derived length and beam of each vessel, accompanied by COG from the preprocessed AIS and VPASS data.

B. Velocity Estimation of Detected Vessels

The velocity and acceleration of target in the SAR antenna coverage modify the slant range between the antenna and the target [39]. As illustrated in (1), the linear term of the equation is imprinted as the physical azimuth shift, where the quadratic term determines the Doppler rate, or azimuth FM rate.

Quantitative influence of the quadratic term of (1) on azimuth FM rate was able to be measured from FrFT-based approach [38], which was implemented in order to measure the azimuth velocity of the vessel from the SAR SLC images. An enhanced mechanism using FrFT-based velocity estimator was introduced, connecting the vessels in the L1C image and the SLC (L1A) image corresponding to them. Mechanisms of the advanced FrFT-based velocity estimation along with the foundation of azimuth FM rate and measurement of velocity through the proposed analysis were consecutively elaborated.

FrFT was considered as a universality of Fourier transform [51], [52]. Fourier transform converts time-series data into frequency domain, in which a peak of moment in time domain was disseminated while influencing every bin of frequency domain. In contrast, FrFT relocates the time domain to joint time-frequency domain, which is defined as a rotation of two-dimensional time-frequency coordinate axes. It implies that i) FrFT signifies joint time-frequency information of different state and phase as the axes rotation angle α is modified and ii) FrFT is reduced into conventional Fourier transform in certain α of $\pi/2$ [39]. A detailed elaboration is demonstrated in (8) and (9), where j, δ and n, respectively, indicates imaginary unit of $\sqrt{-1}$, Dirac delta function and an integer

$$\boldsymbol{F}_\alpha\left(u\right) = \int_{-\infty}^{\infty} \boldsymbol{f}\left(t\right) \boldsymbol{K}_\alpha\left(u,t\right) dt \tag{8}$$

$$\boldsymbol{K}_\alpha\left(u,t\right)$$
$$= \begin{cases} \sqrt{\frac{1-j\cot\alpha}{2\pi}} exp\left(j\frac{u^2+t^2}{2}\cot\alpha - jutcsc\alpha\right), \ \alpha \neq n\pi \\ \boldsymbol{\delta}\left(t-u\right), \ \alpha = 2n\pi \\ \boldsymbol{\delta}\left(t+u\right), \ \alpha = (2n-1)\pi \end{cases}. \tag{9}$$

From (8) and (9), FrFT relocates the time domain signal to rotated domain with given angle α; a particular angle was defined, which concentrates the energy demonstrated on the time-frequency coordinate [38]. In other words, for each range bin containing azimuth profile in SAR image, the target loci was consolidated with respect to a certain angle, which implied the azimuth FM rate determining the target slope in time-frequency

coordinate. Fig. 3 briefly demonstrates the procedure of Fourier transform and FrFT in time-frequency domain containing the target loci.

Under the condition of two-dimensional (2-D) range-azimuth SAR image domain, (8) and (9) derived information both in range and azimuth direction. If a range line was selected to demonstrate an azimuth profile, FrFT was implemented regarding the profile as a 1-D signal, estimating a relationship between pulse repetition frequency and azimuth FM rate [39]. It was implemented vice versa, equation driven between sampling frequency and chirp rate for a range profile. The optimal angle of α_{opt}, which properly concentrates the signal was determined as the maximum value of squared $\boldsymbol{F}_\alpha(u)$, which corresponded to the intensity of SAR SLC image as in

$$\alpha_{opt}, \ u_{opt} = arg \max_{\alpha, \, u} \boldsymbol{F}_\alpha(u)^2. \tag{10}$$

Application of FrFT to range and azimuth profile of SAR SLC data was determined from (11) and (12). Chirp rate and azimuth FM rate are denoted as k_r and k_{az}, where sampling frequency and the number of samples in the profile are demonstrated, respectively, as f_s and N

$$\alpha_{opt_{rng}} = -arctan\left(\frac{f_s^2}{2k_rN}\right) \tag{11}$$

$$\alpha_{opt_{az}} = -arctan\left(\frac{\text{PRF}^2}{2k_{az}N}\right). \tag{12}$$

In [38], a short time FrFT (STFrFT) was implemented as a velocity estimator. This algorithm was regarded as an implementation of short time Fourier transform to FrFT [53]. When Fourier transform dissociates the time-series signal into frequency domain, time information is removed so that the existence of the certain part of the signal with respect to the time axis is left unknown. However, short time Fourier transform applies a window over time-series data and extracts the frequency component within the windowed time [53], [54]. This procedure derived detailed frequency information from the given time component of the window, restoring the target loci in time-frequency domain in Fig. 3(b) from the time-amplitude domain.

Such apparatus was implemented to FrFT on SAR SLC image as the STFrFT-based approach by cropping the azimuth profile into certain length and selecting the part, which contained the signal from vessel. The signals from selected parts were then transformed and annexed to derive a joint time-frequency signal with respect to the selected azimuth profile. This procedure was repeated for every range line and added up to generate the profile with respect to the given rotation angle α.

Unlike the procedure of conventional STFrFT, the methodology in [38] severed and selected the signal containing the vessel from thresholding implementing the mean scattering value of the target vessel. As the target vessel may have the scattering character hardly discernable from the background due to high ocean surface wind or improper heading angle to illuminate the target vessel, an algorithm, which fully employs the azimuth profile while properly suppressing the undesirable ocean scatterers would be necessary. The advanced FrFT-based algorithm,
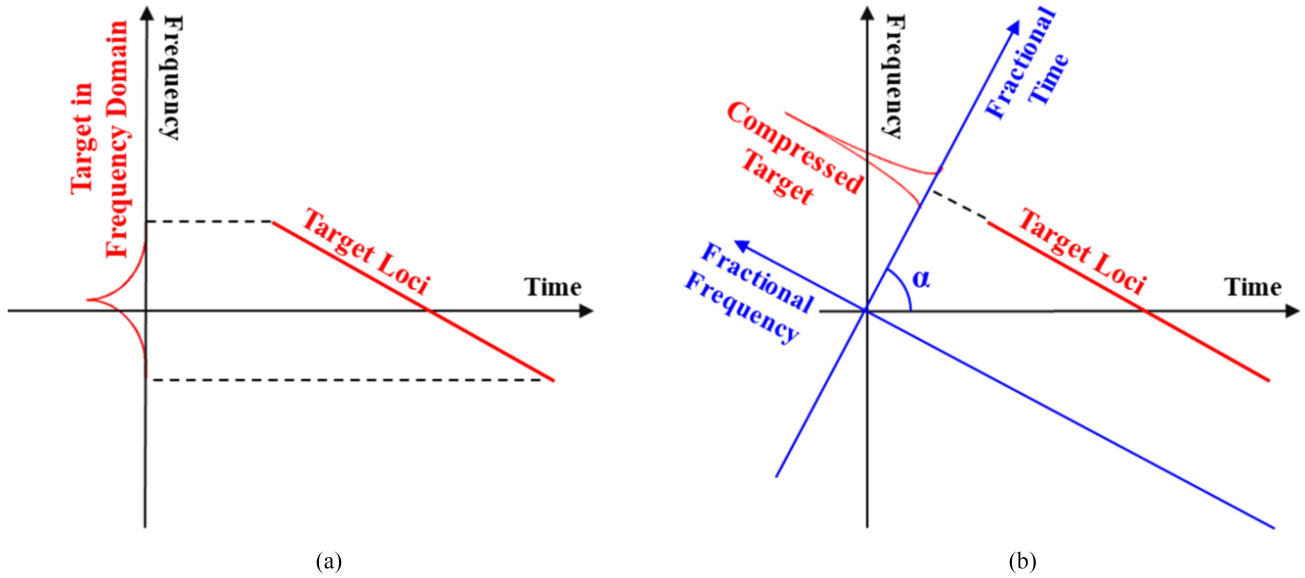
Fig. 3.   Demonstration of target loci in signal time domain both in (a) frequency domain often accompanied by Fourier transform and (b) fractional frequency domain implementing FrFT. While conventional Fourier transform disperse the target loci in frequency domain, FrFT concentrates it in a rotation angle of α.
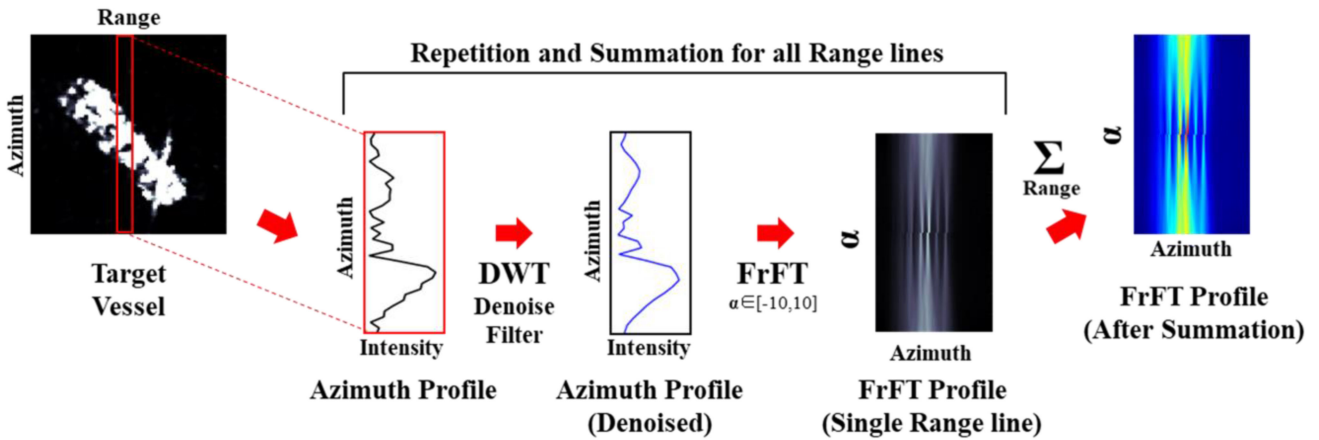

Fig. 4.   Flowchart of the proposed FrFT-based azimuth velocity estimation composed of DWT denoising filter and FrFT operation. The procedure is concluded by accumulating the FrFT profile of every range line in SLC vessel chip.

which adjoined the conventional FrFT velocity estimator and discrete wavelet transform (DWT) noise filter was presented, minimizing the sea scatterers and illuminating the signal from target vessel distinctly.

From the mathematical definition, DWT decomposition noise filter was implemented before the FrFT operation over each azimuth profile. DWT decomposed the signal by consecutively implementing both low-pass filter (LPF) and high-pass filter (HPF); the output coefficients of LPF is called approximation coefficients and that of HPF is called detailed coefficients [55]. Then, the approximation coefficients of the given level were again decomposed by both LPF and HPF. The coefficients, which managed to pass multiple LPFs were defined as the approximation coefficients of the next level, while the other coefficients were regarded as the detailed coefficients, differentiated by the order of HPF application.

In the current application of DWT to azimuth profile of vessels, detailed coefficients of the various levels of operations both contained noise terms from ocean scatterers and momentous changes of signal from the target vessel. As it was necessary to remove the ocean scattering noise instead of that from the vessel, thresholding was implemented, eradicating the value which fail to match the threshold regarding those as noise [56]. The signal after denoising procedure was reconstructed from the approximation coefficients of the given level of operation and the summation of detailed coefficients after thresholding. The sixth-order Symlet (sym6) was implemented as the wavelet, while using the heuristic variant of Stein's unbiased risk estimate as the thresholding apparatus [57].

Fig. 4 describes the brief procedure of operating the proposed FrFT-based velocity estimator. From the cropped chip containing the vessel in SLC image, every azimuth line was extracted

to perform STFrFT for every α, ranging from –10° to 10° with the interval of 0.01° for effective computational cost. During the STFrFT performance, each azimuth profile underwent DWT denoising filter to effectively sort out the signals from oceanic scatterers. FrFT was then performed to the denoised azimuth profile, where the axis demonstrating the azimuth bin moved to the landscape. This procedure was repeatedly implemented for every range line; the output FrFT profiles were accumulated to derive the conclusive FrFT profile. The optimal angle α_{opt}, the angle demonstrating the highest value of FrFT profile intensity, was then selected using (10), from the SLC intensity image. The optimal angle α_{opt} without DWT performance was successively retrieved to compare the performance of the DWT procedure as a reference data.

The SAR image acquisition procedure for each ground or oceanic target was prone to Doppler effect, where the frequency is shifted to some degree due to relative velocity and slant range between the target and platform [58]. For azimuth profile of a SAR image, this character is marked inside by Doppler center frequency and azimuth FM rate. As slant range modification in (1) influenced the Doppler frequency, azimuth FM rate, which contains the moving target was demonstrated by summation of parts; one demonstrating the rate of stationary background, and the other describing the modification caused by the moving target.

In (1), the Doppler centroid along with the rate of stationary target and background was exclusively affected by the slant range; those factors in (1) were eliminated during the performance of azimuth compression, as the azimuth matched filter was generated from Doppler centroid and rate of motionless target [59]. Accordingly, SLC data in Range–Doppler domain indicated the residual Doppler centroid and rate, influenced by moving target velocity. The factor $\frac{y_0 v_{y_0}}{R_0} \eta$ in (1) derived Doppler centroid of the maneuvering target, determined via range velocity component of the target v_{y_0}; it induced the entire target loci to be focused on a shifted position causing the physical azimuth shift in SLC data.

The exact azimuth FM rate for stationary target and maneuvering target is described in (13) and (14), respectively, as k_s and k_m [38], where λ denoting the wavelength of SAR antenna. In addition, the estimation of velocity measurement was conducted on SLC, after the azimuth compression. The azimuth FM rate estimated from SLC is denoted in (15) as follows:

$$k_s = \frac{2v_a^2}{\lambda R_0} \tag{13}$$

$$k_m = \frac{2}{\lambda R_0}\left(-2v_a v_{x_0} + v_{x_0}^2 + v_{y_0}^2\left(1 - \left(\frac{y_0}{R_0}\right)^2\right)\right) + y_0 a_{y_0} \tag{14}$$

$$k_{az} = k_s\left(1 + \frac{k_s}{k_m}\right). \tag{15}$$

In (15), the term k_{az} is estimated, while the terms k_s and k_m are theoretically calculated [39]. By implementing

(12)–(15), the conjunction between FrFT-based velocity estimator and azimuth FM rate was demonstrated as

$$\frac{\text{PRF}^2}{N}\cot\left(\alpha_{opt_{az}}\right)$$

$$= \frac{\left(\frac{2v_a^2}{\lambda R_0}\right)^2}{\frac{2}{\lambda R_0}\left(-2v_a v_{x_0} + v_{x_0}^2 + v_{y_0}^2\left(1 - \left(\frac{y_0}{R_0}\right)^2\right) + y_0 a_{y_0}\right)} + \frac{2v_a^2}{\lambda R_0}. \tag{16}$$

The terms in (14) and (16) contain the velocity of target in range v_{y_0}, azimuth v_{x_0} and range acceleration a_{y_0}. The quadratic term of v_{y_0} contains the ratio $\frac{y_0}{R_0}$, a ratio between ground range and slant rage, equals to $\sin\theta_{inc}$, where θ_{inc} denotes the incidence angle. Hence, the coefficient of $v_{y_0}^2$ becomes $1 - \left(\frac{y_0}{R_0}\right)^2 = \cos^2\theta_{inc}$, ranging from 0 to 1. It was regarded insignificant compared to the coefficients v_a and y_0 and, therefore, was neglected without a loss of generality.

In [38], which previously conducted azimuth velocity extraction from (16), disregarded the term containing a_{y_0} and derived the velocity and separately estimated the influence of acceleration term on velocity estimation. Nevertheless, in order to estimate the effect of a_{y_0} on (16) and verify the possibility to soundly implement the abbreviated equation without the term $y_0 a_{y_0}$ to derive azimuth velocity, both equations with and without the term $y_0 a_{y_0}$ were surmised. The equation deriving azimuth velocity v_{x_0} from the SLC image is demonstrated as in (17), both removing range velocity and range acceleration terms [38]. The equation deriving the azimuth velocity regarding the term of range acceleration $v_{x_0,acc}$, is derived as (18) in the following:

$$v_{x_0} = v_a\left(1 - \sqrt{1 + \frac{2v_a^2}{\lambda R_0\left(\frac{\text{PRF}^2}{N}\right)\cot\left(\alpha_{opt_{az}}\right) - 2v_a^2}}\right) \tag{17}$$

$$v_{x_0,acc} = v_a$$

$$\times\left(1 - \sqrt{1 + \frac{2v_a^2}{\lambda R_0\left(\frac{\text{PRF}^2}{N}\right)\cot\left(\alpha_{opt_{az}}\right) - 2v_a^2} - \frac{y_0 a_{y_0}}{v_a^2}}\right). \tag{18}$$

The azimuth velocity of vessel was estimated both implementing (17) and (18). Evaluation on analyses was conducted using preprocessed AIS and VPASS information corresponding to the target vessel. After deriving the velocity of target vessel on a given SAR acquisition time, a_{y_0} was additionally measured to analyze the effect of range acceleration term in the azimuth velocity estimator. The analyses from (17) and (18) ascertained the practicality of velocity estimation using FrFT and azimuth FM rate estimation. As a_{y_0} was not able to be estimated without v_{x_0}, the proposed algorithm would be regarded practical when little difference was demonstrated between the estimated velocities from (17) and (18).
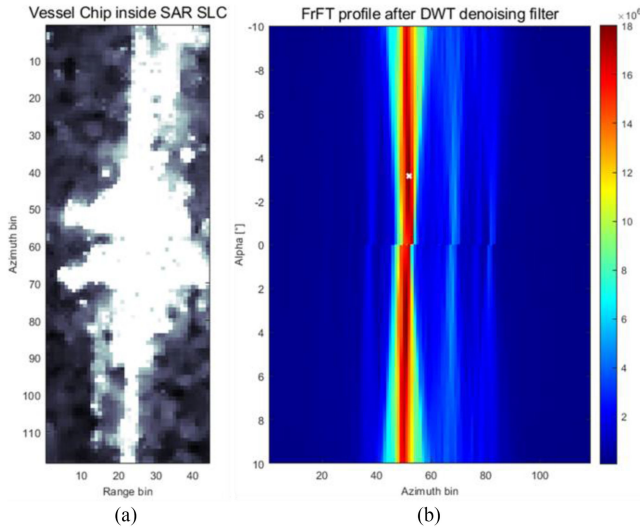
Fig. 5. Typical application of FrFT-based velocity estimator on AIS-equipped vessel. Cropped target vessel from the SLC image is demonstrated as (a), while FrFT-based velocity estimator profile is described as (b). The white index in (b) indicates the azimuth optimal angle $\alpha_{opt_{az}}$.

A typical illustration of FrFT-based velocity estimator is described in Fig. 5, equipped with AIS information applied for verification. The optimal angle for this target vessel is derived as –3.15°, corresponding to the azimuth velocity of 5.25 m/s. The azimuth velocity estimated from AIS information was 5.04 m/s.

C. Restoration of Detected Vessel Position

From the velocity examined from the FrFT-based velocity estimator, the authentic position of the detected vessel was able to be restored by inversely implementing (6). As the slant range and satellite velocity were derived from the state vector, the radial velocity of selected ship ought to be derived from the estimated azimuth velocity from the FrFT operator. The radial velocity v_{y_0}, velocity of the moving target projected to the slant range was expressed as (19) using v_{x_0} and incidence angle θ_i

$$v_{y_0} = v_{x_0} \tan\theta_i \sin\left(\text{COG} - \theta_h\right). \tag{19}$$

The maneuvering direction of the target vessel ought to be identified in order to properly restore the radial velocity. In case where AIS or VPASS information was accompanied, this was derived from preprocessed information. Otherwise, it was to be acquired from assessing the allocation of vessel in the corresponding SAR image. Given that the absolute majority of vessel has its length longer than its beam, Radon transform, which could define the orientation of the object was implemented.

Radon transform is a transform, which reorganizes an image or a distribution into line-projected phase [60]. A polygon or function in Cartesian coordinate $\boldsymbol{f}(x, y)$ is transformed with respect to line prone to the rotation angle θ, to which $\boldsymbol{f}(x, y)$ is projected. The projected domain is demonstrated as x_p, generating the restored domain of $\boldsymbol{Rf}(x_p, \theta)$. The rotation angle of θ is defined initially from the positive y-axis and then counterclockwise. Detailed description of Radon transform was

described in (20), with $\boldsymbol{\delta}$ denotes Dirac Delta function under condition of $0 \leq \theta < 2\pi$

$$\boldsymbol{Rf}(x_p, \theta) = \int_{-\infty}^{\infty} \int_{-\infty}^{\infty} \boldsymbol{f}(x, y) \, \boldsymbol{\delta}(x_p - x\cos\theta - y\sin\theta) \, dxdy. \tag{20}$$

With respect to the orientation angle, where the signal from target vessel is expected to be concentrated, $\boldsymbol{Rf}(x_p, \theta)$ demonstrates the highest amplitude and the narrowest scope accordingly. From the presumption of vessel appearance, the angle illustrating the highest value after Radon transform of vessel in the SLC image was regarded as COG or COG+π. This ambiguity depends on the allocation of vessel on a given direction, whether the vessel is maneuvering onward or backward.

After the ascertainment of orientation, the mitigation of target vessel was resolved from (2) and (19). Notwithstanding, the ambiguity of π would be able to induce an undesirable counter offset. This issue was eliminated by sorting out one of the two candidates; as the signal of vessel represents high backscattering features in ocean, low backscattering regions, allegedly determined as ocean without the vessel, or high backscattering region on ground, which contains altitude information from digital elevation model (DEM). Hence, the candidates on land were first removed by implementing DEM, followed by a selection of candidate demonstrating higher backscattering coefficient.

IV. RESULTS

The analyses on identification, velocity estimation, orientation measurement, and azimuth shift correction were implemented to the test SAR images presented in Table I. As false-alarms could act as a bottleneck in both analyses, dropping the identification rate and the assessment of velocity estimator, the CNN-based detector demonstrating higher precision than recall was preferred.

In order to compare the detection output with preprocessed AIS and VPASS information, the bounding box constructed from AIS and VPASS information was applied and assessed by measuring the overlap to the detection output. This was conducted and evaluated by IoU as in (7); the detection output, which demonstrated the IoU rate over certain threshold with any AIS/VPASS-based bounding box was regarded as a vessel operating with AIS or VPASS sensor activated. In previous studies in object detection, the IoU threshold, which determined the accurate detection was often implemented as 0.5 [61]. In addition, SAR image-based vessel detector otherwise resolved the value as 0.2, given the possibility of low spatial resolution and relatively small targets than that of conventional object detection [21].

In this condition, where IoU was implemented to discern the unidentified vessels from superposition of AIS and VPASS information over the detection output, the threshold, which separates the identified vessel from the others was selected as 0.2. Namely, the detection output demonstrating higher value of IoU than 0.2 over one or more reference box from AIS and VPASS was regarded as a vessel operating either AIS or VPASS information and accordingly recognized identified. In contrast, the detection output, which failed to match such
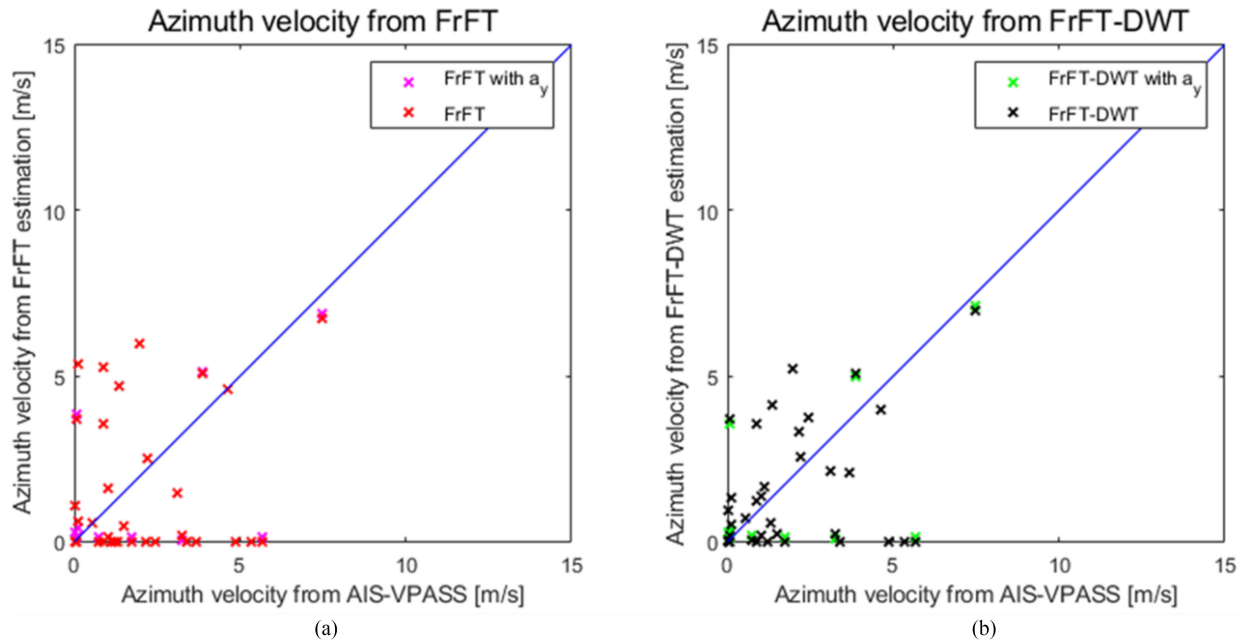
Fig. 6. Demonstration of azimuth velocity estimation in four different conditions. The blue line indicates the ideal estimation of azimuth velocity. The measurement from FrFT-based velocity estimator was illustrated in (a), where indicators in magenta and red describe the azimuth velocity with and without considering range acceleration respectively. Velocity estimation both implementing FrFT and DWT denoising filter was demonstrated in (b), where green and black indicators describe the velocity with and without considering range acceleration.

TABLE III
VESSEL IDENTIFICATION FROM 3 SAR IMAGES AND CORRESPONDING
AIS/VPASS INFORMATION

Acquisition Date	Detected Vessels	Unidentified Vessels	Unidentification rate [%]
Overall	**132**	**39**	**29.54**
04/03/2018	46	8	17.89
22/07/2018	44	17	38.63
14/10/2018	42	14	33.33

condition was regarded otherwise. Given the legal regulations, which coerce to activate AIS or VPASS device of vessel [43], the latter was regarded unidentified, involving a potential hazard of illegitimate actions. The performance of vessel identification procedure on Cosmo-SkyMed SAR images is demonstrated as in Table III.

The velocity estimation followed by the restoration of authentic vessel position was primarily intended to be implemented to unidentified vessel of which the movement could not be monitored via AIS and VPASS information. Paradoxically, however, the assessment was only operated to the identified vessels accompanied by AIS or VPASS information, since it was a sole reference for comparison. On the identified vessels, an assessment on three different aspects was made: 1) accuracy of velocity measurement, 2) accuracy of estimating COG, and 3) accuracy of authentic position restoration.

The assessment on the velocity estimation was conducted by comparing the output of FrFT-based velocity estimator with and without DWT noise filter in addition to the measurement of a_{y_0} on deriving v_{x_0}. This evaluation was conducted in regard

to the usage of position restoration; the vessels maneuvering parallel to the azimuth or range direction were disregarded. The vessels moving in line with the satellite would demonstrate zero range velocity and therefore no azimuth shift to restore, while those moving in range direction would be the most dominantly influenced by azimuth shift in given velocity but theoretically display no azimuth velocity from FrFT-based velocity estimator. For such reason, vessels in azimuth or range direction with 7° of allowance scope were removed from assessment. The vessels in near-harbor regions were additionally removed; there was a high possibility that the target Doppler frequency was unfavorably influenced by the signal from the harbor in addition to the fact that the vessels in near-harbor regions were often docked in the port.

Fig. 6 describes the evaluation of velocity estimation on both aspect of DWT and range acceleration. When the conventional FrFT velocity estimator without DWT filter was implemented, mean and median value of velocity offset were estimated as 1.65 m/s and 1.04 m/s. When the range acceleration term was given into consideration mean and median velocity offset were demonstrated as 1.64 m/s and 1.04 m/s. In contrast, in case of employing the advanced FrFT-based velocity detector, mean, and median value of velocity offset were surmised as 1.29 m/s and 0.78 m/s; when range acceleration considered, those were calculated as 1.27 m/s and 0.78 m/s, respectively. Analogous procedure was conducted from STFrFT, deriving azimuth velocity of target vessel from (17) [38]. It illustrated 2.75 m/s of mean absolute offset.

The estimation of COG from Radon transform was tested against the COG from preprocessed AIS and VPASS information. It also omitted the vessels aligned in vicinity of azimuth and
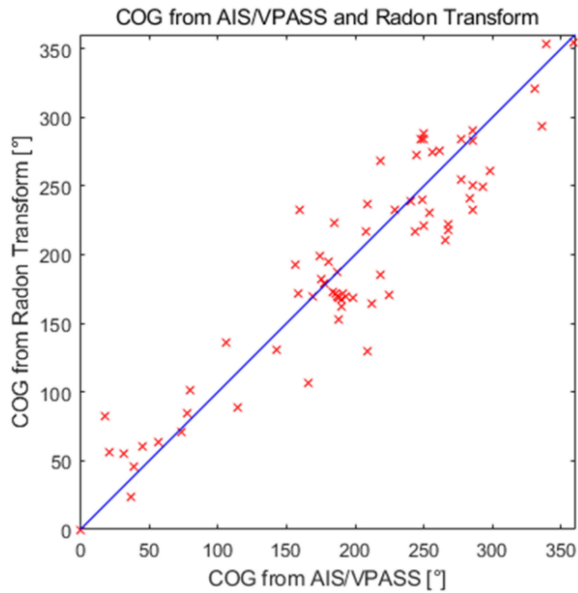
Fig. 7. Contrast between COG derived from preprocessed AIS/VPASS information and Radon transform. The blue line indicates the ideal estimation of orientation implementing Radon transform.

range direction with respect to COG from preprocessed AIS and VPASS information with allowance of 7°. The mean offset angle between the two COG derivations was 25.1° from 52 vessels. Fig. 7 demonstrates the difference between vessel orientation angles from preprocessed AIS/ VPASS information and Radon transform.

The determinative assessment of restoring the authentic position of vessel was conducted implementing both datasets in previous evaluations. Implementing the derived azimuth velocity from FrFT-based velocity estimator accompanied by DWT denoising filter along with the COG derived from Radon Transform, the expected azimuth shift was estimated via (6). As the analysis restored the azimuth shift from velocity from FrFT-based velocity estimator and orientation from Radon Transform, the reference azimuth shift was restored from preprocessed AIS and VPASS information, exploiting COG and SOG from it respectively. The restored quantity of azimuth shift was demonstrated in Fig. 8, which was tested against the reference azimuth shift generated from preprocessed COG and SOG. As the velocity estimation of vessel was operated in four different cases, the measurement of azimuth shift was conducted on such basis; azimuth velocity with and without range acceleration term and DWT denoising filter each determined different quantity of azimuth shift. Trimmed mean of 10% azimuth shift error from the velocity measured from FrFT with and without considering range acceleration, respectively, yielded 70.69 m and 70.75 m of offset, while that from the proposed conjoined measurement of FrFT and DWT demonstrated 61.93 m and 62.39 m of azimuth offset.

V. DISCUSSION

SAR image-based vessel detection implementing CNN-based object detector achieved a number of advancements in terms

of ameliorating the performance; while a majority of studies focused on introducing the detector algorithms with higher accuracy [16]–[19], the others attempted to generate a database containing vessel chip, or an algorithm, which rendered a robust training data of vessel from AIS information [20], [21]. Nevertheless, while implementing the CNN-based vessel detector, which was previously elaborated, identification of vessels along with the demonstration of authentic position of vessels was presented. Accomplishment of such analyses was executed from conventional apparatus regarding vessel detection and surveillance: SAR-AIS data fusion [22], Doppler parameter extraction for velocity measurement in single-channeled SAR data [39], [58], and explicit preprocessing of AIS information [21].

The assessment of identification procedure was conducted to three SAR images, which contain the vessel detection output. The temporal acquisition condition of the test SAR images as in Table I was distinctive with one another, the identification rate was not consistent within the images though containing identical spatial coverage. The average identification rate in the three Cosmo-SkyMed images indicated 70.46% while excluding the vessels left inactive; such vessels were often spared from the regulations of AIS/VPASS sensor guidance [43].

Different analyses implementing two velocity estimation algorithm, conventional FrFT and the proposed FrFT-based velocity estimator, with (17) and (18) were performed and assessed in order to measure i) the performance of the suggested FrFT-based velocity estimator accompanied by DWT denoising filter and ii) the effect of range acceleration on azimuth velocity estimation. The absolute mean velocity offset estimated from the proposed algorithm decreased with respect to that from the conventional velocity estimation from [38]. The performance of advanced FrFT-based velocity estimator was demonstrated, showing both absolute mean and median velocity of offset 1.29 m/s and 0.78 m/s ameliorated than that from the conventional FrFT estimator of 1.65 m/s and 1.04 m/s. The velocity offset decreased significantly, which implied that DWT denoising filter soundly operated in removing detrimental noise signals from oceanic scatterers. In addition, both of the operations implementing acceleration terms illustrated around 0.01 m/s improvements compared to that without considering range accelerations. The decrease in absolute mean velocity offset was regarded as trivial compared to the enhancement from implementation of the DWT denoising filter. Moreover, vessels whose precision of estimated velocity was ameliorated were irrelevant to range angle. This indicated that vessels with high range acceleration did not demonstrate an absolute mean velocity offset enhancement. Given that the range acceleration term for (18) was originated from preprocessed AIS and VPASS information, derivation of $v_{x_0,acc}$ was impossible for vessels without AIS and VPASS information, or unidentified vessels. Fig. 6 suggested that the range acceleration had little effect on performance enhancement of azimuth velocity estimation. From such analyses where azimuth FM rate was near comprehensively determined by azimuth velocity, it was verified that (17) was able to substitute (18) for practical usages without a loss of generality. The insignificant influence of range acceleration on azimuth velocity was furthermore ascertained in measuring azimuth shift
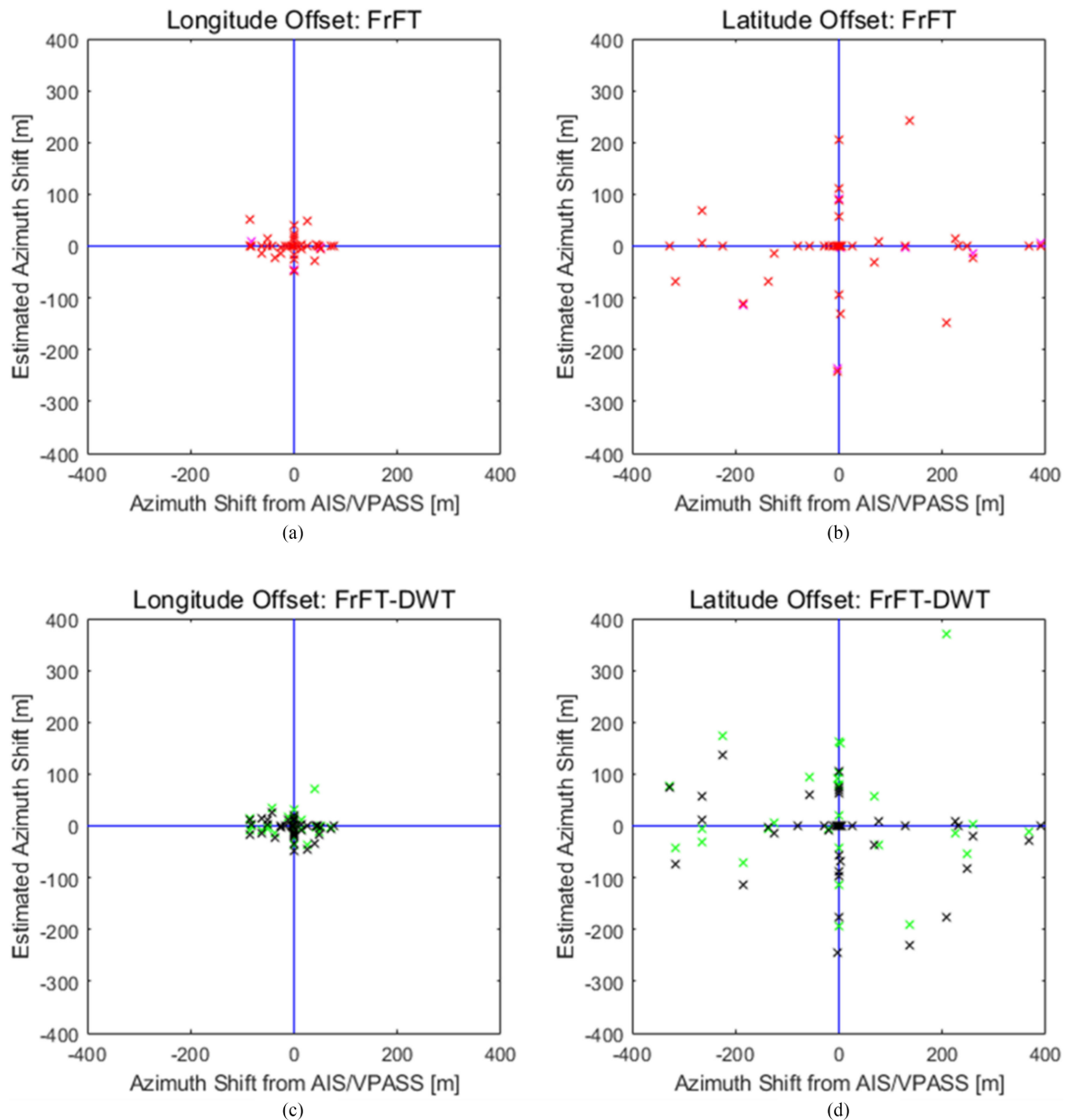
Fig. 8. Comparison between the azimuth shift restored from AIS/VPASS information and the velocity estimator accompanied by Radon transform. Indications in magenta and red each demonstrates velocity driven by FrFT operator, with and without regarding range acceleration terms; the shift was dissolved in longitude (a) and latitude (b). Green and black indication, respectively, elaborates velocity driven by FrFT operator accompanied by DWT denoising filter, with and without regarding range acceleration terms; the shift was dissolved in longitude (c) and latitude (d).

in Fig. 8. The average mismatch of estimated azimuth shift with and without examination of range acceleration was negligible; in case of implementation of DWT in velocity estimation, however, it demonstrated an enhancement in identical procedure, where the mean mismatch reduced approximately 8 m.

Fig. 9 describes a typical example of restoring the azimuth shift from velocity derived implementing (17). In the case, the range velocity transformed from the azimuth velocity was 5.73 m/s, while the range velocity from preprocessed AIS information was 5.78 m/s. From the analytic formula of (2) regarding the quantity of azimuth shift, the two different cases presented 263.02 m and 264.86 m of azimuth shift each, as the slant range

and the Cosmo-SkyMed satellite velocity were fixed to 710,197 m and 7600 m/s, respectively

A majority of studies on vessel velocity estimation in single-channeled SAR images depended on measuring the distance between the vessel signatures and corresponding vessel wakes in order to derive the quantity of physical azimuth shift driven by Doppler centroid of moving target [62]–[66]. This procedure, however, was replaced by FrFT-based azimuth velocity estimator for several reasons below. First of all, the complete signatures of vessel wake were not often visible in single SAR acquisition condition. As the significant wave height increased, the detectability of vessel wake diminished linearly [68]. In contrast to
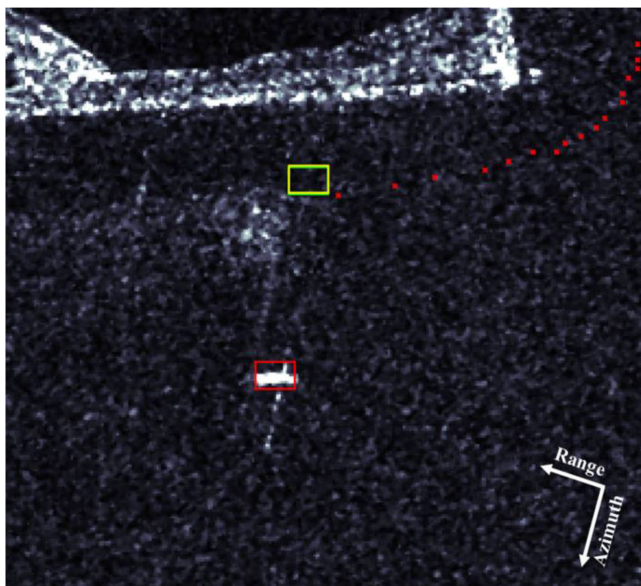
Fig. 9. Example of restoring the genuine position of bounding box in L1C SAR image from the azimuth velocity estimator. The red box depicts the bounding box influenced by azimuth shift, while the green and yellow box respectively describes that after restoration using estimated velocity from the azimuth velocity estimator and AIS information. The red indexes depict the vessel position from AIS information.

the solid vessel signature of which the scattering characteristics were seldom influenced by inhospitable weather conditions, wake detection demanded fastidiously tranquil circumstances for sound operation. In addition, the wake signature was comprised of several constituent wakes such as transverse, divergent and turbulent wakes, which renders it difficult to properly discern the general character of the vessel wake [69]. Last but not least, the wake signature was physically invisible in cross-polarization conditions; even those in horizontal and vertical polarization demonstrated a tradeoff between left and right arms of wake in terms of observability [70]. Given such restrictions, derivation of radial velocity from the azimuth velocity estimator was operated, even though the azimuth shift measurement of vessel aligned to range direction was impossible from such analysis.

The analyses presented in this article proposed the algorithm, which was able to be implemented to restoration of authentic position of unidentified vessel, by presenting 1) an advanced vessel identification algorithm by matching the vessel detection output to AIS/VPASS information followed by 2) demonstrating the authentic position of vessels from restoration of azimuth velocity and maneuvering direction from vessel signature. In contrast, current study engendered handful of unresolved academic issues related to this field. The velocity derived from the advanced FrFT-based detector illustrated was azimuth velocity; restoring the authentic velocity of vessel without implementing range velocity term would be insufficient. As the range velocity component could be measured by estimating azimuth shift in (2), range velocity measurement is imperative in order to implement a robust vessel velocity reconstruction. In addition, feasible implementation of vessel identification and velocity estimation demands a high performance CNN-based vessel detector,

especially of which the precision is nearly perfected. For such objective, an up-to-date vessel detector algorithm trained under different SAR satellite conditions was imperative. Successive academic attempts regarding this issue could be able to concentrate on resolving these issues. The identification algorithm could be applied identically to other remote sensing platforms, such as EO and infrared satellite or airborne sensor images.

VI. CONCLUSION

Aside from the conventional analyses on vessel detection directed to performance refinement and database generation, this article focused on reestablishment of authentic position of vessel without influence of azimuth shift, which could be implemented to the vessels outside the coverage of vessel surveillance apparatus. The evaluation of two presented algorithms was performed on the test SAR images containing vessel detection output, deriving the identification rate and estimated velocity which was tested against the velocity from AIS and VPASS information. The identification rate was derived for each test SAR image, respectively, and the accuracy of estimated velocity from the proposed FrFT-based velocity detector significantly exceeded that of conventional FrFT velocity estimation algorithm; from 1.65 m/s to 1.29 m/s in mean azimuth velocity estimation offset and from 70.75 m to 62.39 m in average azimuth shift estimation. The output of this article eventually derived that the analyses were applicable without considering range acceleration terms. As these analyses could be implemented identically in other remote sensing apparatus for vessel detection, successive studies may contain a thorough extraction of vessel velocity by restoring the range component.

REFERENCES

[1] P. Vachon, J. Campbell, C. Bjerkelund, F. Dobson, and M. Rey, "Ship detection by the RADARSAT SAR: Validation of detection model predictions," *Can. J. Remote Sens.*, vol. 23, no. 1, pp. 48–59, Mar. 1997.

[2] M. Liao, C. Wang, Y. Wong, and L. Jiang, "Using SAR images to detect ships from sea clutter," *IEEE Geosci. Remote Sens. Lett.*, vol. 5, no. 2, pp. 194–198, Apr. 2008.

[3] Y. Wang, Z. Zhang, N. Li, F. Hong, H. Fan, and X. Wang, "Maritime surveillance with undersampled SAR," *IEEE Geosci. Remote Sens. Lett.*, vol. 14, no. 8, pp. 1423–1427, Jul. 2017.

[4] M. Stasolla, J. Mallorquí, G. Margarit, C. Santamaria, and N. Walker, "A comparative study of operational vessel detectors for maritime surveillance using satellite-borne synthetic aperture radar," *IEEE J. Sel. Topics Appl. Earth Observ. Remote Sens.*, vol. 9, no. 6, pp. 2687–2701, Jun. 2016.

[5] H. Li, W. Perrie, Y. He, S. Lehner, and S. Brusch, "Target detection on the ocean with the relative phase of compact polarimetry SAR," *IEEE Trans. Geosci. Remote Sens.*, vol. 51, no. 6, pp. 3299–3305, Jun. 2013.

[6] Q. Zhang, J. Wu, L. Zhongyu, Y. Miao, Y. Huang, and J. Yang, "PFA for bistatic forward-looking SAR mounted on high-speed maneuvering platforms," *IEEE Trans. Geosci. Remote Sens.*, vol. 57, no. 8, pp. 6018–6036, Apr. 2019.

[7] J. Truckenbrodt *et al.*, "Towards sentinel-1 SAR analysis-ready data: A best practices assessment on preparing backscatter data for the cube," *Data*, vol. 4, no. 3, Jul. 2019, Art. no. 93.

[8] Z. Zhang, H. Wang, F. Xu, and Y Jin, "Complex-valued convolutional neural network and its application in polarimetric SAR image classification," *IEEE Trans. Geosci. Remote Sens.*, vol. 55, no. 12, pp. 7177–7188, Dec. 2017.

[9] S. Chen, H. Wang, F. Xu, and Y. Jin, "Target classification using the deep convolutional networks for SAR images," *IEEE Trans. Geosci. Remote Sens.*, vol. 54, no. 8, pp. 4806–4817, Jun. 2016.

[10] H. Park, S. Park, and Y. Joo, "Detection of abandoned and stolen objects based on dual background model and mask R-CNN," *IEEE Access*, vol. 8, pp. 80010–80019, Apr. 2020.

[11] A. Zhang, X. Yang, S. Fang, and J. Ai, "Region level SAR image classification using deep features and spatial constraints," *ISPRS J. Photogrammetry Remote Sens.*, vol. 163, pp. 36–48, May 2020.

[12] Z. Zhao, K. Ji, X. Xing, H. Zou, and S. Zhou, "Ship surveillance by integration of space-borne SAR and AIS-review of current research," *J. Navigation*, vol. 67, no. 1, pp. 177–189, Jan. 2013.

[13] R. Wang, J. Li, Y. Duan, H. Cao, and Y. Zhao, "Study on the combined application of CFAR and deep learning in ship detection," *J. Indian Soc. Remote. Sens.*, vol. 46, pp. 1413–1421, Jun. 2018.

[14] S. Zhang, R. Wu, K. Xu, J. Wang, and W. Sun, "R-CNN-based ship detection from high resolution remote sensing imagery," *Remote Sens*, vol. 11, no. 6, Mar. 2013, Art. no. 631.

[15] L. Qi *et al.*, "Ship target detection algorithm based on improved faster R-CNN," *Electron*, vol. 8, no. 9, Aug. 2019, Art. no. 959.

[16] H. Li, L. Deng, C. Yang, J. Liu, and Z. Gu, "Enhanced YOLO v3 tiny network for real-time ship detection from visual image," *IEEE Access*, vol. 9, pp. 16692–16706, Jan. 2021.

[17] G. Tang, S. Liu, I. Fujino, C. Claramunt, Y. Wang, and S. Men, "H-YOLO: A single-shot ship detection approach based on region of interest preselected network," *Remote Sens.*, vol. 12, no. 24, Dec. 2020, Art. no. 4192.

[18] J. Wang, T. Zheng, P. Lei, and X. Bai, "A hierarchical CNN-based ship target detection method in spaceborne SAR imagery," *Remote Sens.*, vol. 11, no. 6, Mar. 2019, Art. no. 620.

[19] T. Zhang and X. Zhang, "High-speed ship detection in SAR images based on a grid CNN," *Remote Sens.*, vol. 11, no. 10, May 2019, Art. no. 1206.

[20] L. Huang *et al.*, "OpenSARShip: A dataset dedicated to sentinel-1 ship interpretation," *IEEE J. Sel. Topics Appl. Earth Observ. Remote Sens.*, vol. 11, no. 1, pp. 195–208, Jan. 2018.

[21] J. Song, D. Kim, and K. Kang, "Automated procurement of training data for machine learning algorithm on ship detection using AIS information," *Remote Sens.*, vol. 12, no. 9, May 2020, Art. no. 1443.

[22] R. Pelich, N. Longépé, G. Mercier, G. Hajduch, and R. Garello, "AIS-based evaluation of target detectors and SAR sensors characteristics for maritime surveillance," *IEEE J. Sel. Topics Appl. Earth Observ. Remote Sens.*, vol. 8, no. 8, pp. 3892–3901, Aug. 2015.

[23] A. Kurekin *et al.*, "Operational monitoring of illegal fishing in Ghana through exploitation of satellite earth observation and AIS data," *Remote Sens.*, vol. 11, no. 3, Feb. 2019, Art. no. 293.

[24] A. Czapiewska and J. Sadowski, "Algorithms for ship movement prediction for location data compression," *Int. J. Mar. Navigation Saf. Sea Trans.*, vol. 9, no. 1, pp. 75–81, Mar. 2015.

[25] K. Jaskolski, "AIS dynamic data estimation based on discrete Kalman filter algorithm," *Sci. J. Pol. Navigation Acad.*, vol. 4, no. 211, pp. 71–87, Dec. 2017.

[26] L. Jia, M. Li, P. Zhang, Y. Wu, and H. Zhu, "SAR image change detection based on multiple kernel K-means clustering with local-neighborhood information," *IEEE Geosci. Remote Sens. Lett.*, vol. 13, no. 6, pp. 856–860, Jun. 2016.

[27] E. Makhoul, A. Broquetas, J. Ruiz-Rodon, Y. Zhan, and F. Ceba, "A performance evaluation of SAR-GMTI mission for maritime applications," *IEEE Trans. Geosci. Remote Sens.*, vol. 53, no. 5, pp. 2409–2509, May 2015.

[28] S. Baumgartner and G. Krieger, "Fast GMTI algorithm for traffic monitoring based on a priori knowledge," *IEEE Trans. Geosci. Remote Sens.*, vol. 50, no. 11, pp. 4626–4641, Nov. 2012.

[29] C. Gierull, I. Sikaneta, and D. Cerutti-Maori, "Two-step detector for RADARSAT-2's experimental GMTI mode," *IEEE Trans. Geosci. Remote Sens.*, vol. 51, no. 1, pp. 436–454, Jan. 2013.

[30] L. Lightstone, D. Faubert, and G. Rempel, "Multiple phase centre DPCA for airborne radar," in *Proc. IEEE Nat. Radar Conf.*, 1991, pp. 36–40.

[31] J. Xu, Z. Huang, L. Yan, X. Zhou, F. Zhang, and T. Long, "SAR ground moving target indication based on relative residue of DPCA processing," *Sensors*, vol. 16, no. 10, Oct. 2016, Art. no. 1676.

[32] G. Gao and G. Shi, "Ship detection in dual-channel ATI-SAR based on the notch filter," *IEEE Trans. Geosci. Remote Sens.*, vol. 55, no. 8, pp. 4795–4810, Aug. 2017.

[33] J. Li, Y. Huang, G. Liao, and J. Xu, "Moving target detection via efficient ATI-GoDec approach for multichannel SAR system," *IEEE Trans. Geosci. Remote Sens.*, vol. 13, no. 9, pp. 1320–1324, Sep. 2016.

[34] D. Ao, M. Datcu, G. Schwarz, and C. Hu, "Moving ship velocity estimation using TanDEM-X data based on subaperture decomposition," *IEEE Geosci. Remote Sens. Lett.*, vol. 15, no. 10, pp. 1560–1564, Oct. 2018.

[35] C. Wang, P. Shen, X. Li, J. Zhu, and Z. Li, "A novel vessel velocity estimation method using dual-platform TerraSAR-X and TanDEM-X full polarimetric SAR data in pursuit monostatic mode," *IEEE Trans. Geosci. Remote Sens.*, vol. 57, no. 8, pp. 6130–6144, Aug. 2019.

[36] J. Xu, G. Li, Y. Peng, X. Xia, and Y. Wang, "Parametric velocity synthetic aperture radar: Multilook processing and its applications," *IEEE Trans. Geosci. Remote Sens.*, vol. 46, no. 11, pp. 3488–3502, Nov. 2008.

[37] K. Ouchi, "On the multi-look images of moving targets by synthetic aperture radars," *IEEE Trans. Antennas Propag.*, vol. 33, no. 8, pp. 823–827, Aug. 1985.

[38] R. Pelich, N. Longépé, G. Mercier, G. Hajduch, and R. Garello, "Vessel refocusing and velocity estimation on SAR imagery using the fractional fourier transform," *IEEE Trans. Geosci. Remote Sens.*, vol. 54, no. 3, pp. 1670–1684, Mar. 2016.

[39] C. Chen, Y. Li, K. Huang, Y. Long, L. Zhang, and K. Ouyang, "Ship velocity estimation in airborne along-track interferometric SAR imagery based on the fractional fourier transform," *Int. J. Antennas Propag.*, vol. 2020, Nov. 2020, Art. no. 5835620.

[40] S. Chiu, "Application of fractional fourier transform to moving target indication via along-track interferometry," *EURASIP J. Adv. Signal Process.*, vol. 20, pp. 3293–3303, Dec. 2005.

[41] L. Almeida, "The fractional fourier transform and time-frequency representations," *IEEE Trans. Signal Process.*, vol. 42, no. 11, pp. 3084–3091, Nov. 1994.

[42] R. Pelich *et al.*, "Large-scale automatic vessel monitoring based on dual-polarization Sentinel-1 and AIS data," *Remote Sens.*, vol. 11, no. 9, May 2019, Art. no. 1078.

[43] M. Lee, Y. Park, S. Park, E. Lee, M. Park, and N. Kim, "Application of collision warning algorithm alarm in fishing vessel's waterway," *Appl. Sci.*, vol. 11, no. 10, May 2021, Art. no. 4479.

[44] H. Lang, H. Wu, and Y. Xu, "Ship classification in SAR images improved by AIS knowledge transfer," *IEEE Geosci. Remote Sens. Lett.*, vol. 15, no. 3, pp. 439–443, Jan. 2018.

[45] J. Wang *et al.*, "Doppler shift estimation for space-based AIS signals over satellite-to-ship links," *IEEE Access*, vol. 7, pp. 76250–76262, Jun. 2019.

[46] L. Sang, A. Wall, Z. Mao, X. Yan, and J. Wang, "A novel method for restoring the trajectory of the inland waterway ship by using AIS data," *Ocean Eng.*, vol. 110, pp. 183–194, Dec. 2015.

[47] J. Yang, X. Qiu, M. Shang, S. Lv, L. Zhong, and C. Ding, "Radial velocity estimation of ships on open sea in the azimuth multichannel SAR system," *IEEE J. Sel. Topics Appl. Earth Observ. Remote Sens.*, vol. 14, pp. 3787–3798, Mar. 2021.

[48] P. Sengupta, S. Vadali, and K. Alfriend, "Satellite orbit design and maintenance for terrestrial coverage," *J. Spacecraft Rockets*, vol. 47, no. 1, pp. 177–187, Jan. 2010.

[49] A. Bochkovskiy, C. Wang, and H. Liao, "YOLOv4: Optimal speed and accuracy of object detection," 2020, *arXiv:2004.10934*.

[50] M. Rezaei and M. Azarmi, "DeepSOCIAL: Social distancing monitoring and infection risk assessment in COVID-19 pandemic," *Appl. Sci.*, vol. 10, no. 21, Oct. 2020, Art. no. 7514.

[51] D. Mendlovic, Z. Zalevsky, D. Mas, J. Garcia, and C. Ferreira, "Fractional wavelet transform," *Appl. Opt.*, vol. 36, no. 20, pp. 4801–4806, Jul. 1997.

[52] H. Ozaktas, O. Arikan, M. Kutay, and G. Bozdaki, "Digital computation of the fractional fourier transform," *IEEE Trans. Signal Process.*, vol. 44, no. 9, pp. 2141–2150, Sep. 1996.

[53] S. Pei and J. Ding, "Relations between gabor transforms and fractional fourier transforms and their applications for signal processing," *IEEE Trans. Signal Process.*, vol. 55, no. 10, pp. 4839–4850, Sep. 2007.

[54] M. Unser, "Fast Gabor-like windowed fourier and continuous wavelet transforms," *IEEE Signal Process. Lett.*, vol. 1, no. 5, pp. 76–79, May 1994.

[55] M. Lang, H. Guo, J. Odegard, C. Burrus, and R. Wells, "Noise reduction and undecimated discrete wavelet transform," *IEEE Signal Process. Lett.*, vol. 3, no. 1, pp. 10–12, Jan. 1996.

[56] J. Fowler, "The redundant discrete wavelet transform and additive noise," *IEEE Signal Process. Lett.*, vol. 12, no. 9, pp. 629–632, Sep. 2005.

[57] D. Donoho, "De-noising by soft-thresholding," *IEEE Trans. Inf. Theory.*, vol. 41, no. 3, pp. 613–627, May 1995.

[58] K. Kang, D. Kim, S. Kim, and W. Moon, "Doppler velocity characteristics during tropical cyclones observed using ScanSAR raw data," *IEEE Trans. Geosci. Remote Sens.*, vol. 54, no. 4, pp. 2343–2355, Jan. 2016.

[59] J. Won, "A quick-and-dirty method for detection of ground moving targets in single-channel SAR single-look complex (SLC) images by differentiation," *Korean J. Remote Sens.*, vol. 30, no. 2, pp. 185–205, Mar. 2014.

[60] G. Rigaud, J. Bellet, G. Berginc, I. Berechet, and S. Berechet, "Reflective imaging solved by the radon transform," *IEEE Geosci. Remote Sens. Lett.*, vol. 13, no. 7, pp. 936–938, Jul. 2016.

[61] S. Gidaris and N. Komodakis, "LocNet: Improving localization accuracy for object detection," in *Proc. IEEE Conf. Comput. Vis. Pattern Recognit.*, 2016, pp. 789–798.

[62] K. Kang and D. Kim, "Ship velocity estimation from ship wakes detected using convolutional neural networks," *IEEE J. Sel. Topics Appl. Earth Observ. Remote Sens.*, vol. 12, no. 11, pp. 4379–4388, Nov. 2019.

[63] M. Graziano, M. D'Errico, and G. Rufino, "Wake component detection in X-band SAR images for ship heading and velocity estimation," *Remote Sens.*, vol. 8, no. 6, Jun. 2016, Art. no. 498.

[64] M. Dragosevic and P. Vachon, "Estimation of ship radial speed by adaptive processing of RADARSAT-1 fine mode data," *IEEE Geosci. Remote Sens. Lett.*, vol. 5, no. 4, pp. 678–682, Oct. 2008.

[65] A. Renga and A. Moccia, "Use of doppler parameters for ship velocity computation in SAR images," *IEEE Trans. Geosci. Remote Sens.*, vol. 54, no. 7, pp. 3995–4011, Jul. 2016.

[66] J. Li, L. Wang, M. Zhang, Y. Jiao, and G. Liu, "Ship velocity automatic estimation method via two-dimensional spectrum pattern of kelvin wakes in SAR images," *IEEE J. Sel. Topics Appl. Earth Observ. Remote Sens.*, vol. 14, pp. 4779–4786, Apr. 2021.

[67] G. Zilman, A. Zapolski, and M. Marom, "The speed and beam of a ship from its wake's SAR images," *IEEE Trans. Geosci. Remote Sens.*, vol. 42, no. 10, pp. 2335–2343, Oct. 2004.

[68] G. Zilman, A. Zapolski, and M. Marom, "On detectability of a ship's kelvin wake in simulated SAR images of rough sea surface," *IEEE Trans. Geosci. Remote Sens.*, vol. 53, no. 2, pp. 609–619, Feb. 2015.

[69] Y. Sun and Y. Jin, "Ship wake components: Isolation, reconstruction, and characteristics analysis in spectral, spatial, and TerraSAR-X image domains," *IEEE Trans. Geosci. Remote Sens.*, vol. 56, no. 7, pp. 4209–4224, Jul. 2018.

[70] A. Panico, M. Graziano, and A. Renga, "SAR-based vessel velocity estimation from partially imaged Kelvin pattern," *IEEE Geosci. Remote Sens. Lett.*, vol. 14, no. 11, pp. 2067–2071, Nov. 2017.

Duk-jin Kim (Senior Member, IEEE) received the B.Sc. degree in earth system science and the M.Sc. and Ph.D. degrees in radar remote sensing and geophysics from Seoul National University, Seoul, South Korea, in 1999, 2001, and 2005, respectively.

From October 2005 to July 2007, he was a Postdoctoral Researcher with the University of Manitoba, Winnipeg, MB, Canada, and with the University of Michigan, Ann Arbor, MI, USA. From July 2007 to August 2008, he was a Senior Researcher with the Remote Sensing Division, Korea Aerospace Research Institute, Daejeon, South Korea. He is currently a Full Professor with the School of Earth and Environmental Sciences, Seoul National University. During his sabbatical leave from August 2014 to July 2015, he was a Visiting Scholar with the Radar Science and Engineering Section, Jet Propulsion Laboratory, California Institute of Technology, Pasadena, CA, USA. His research interests include coastal environment and disaster monitoring using space-borne and airborne synthetic aperture radar (SAR) systems, as well as ocean/sea ice parameter extractions using along-track interferometric and polarimetric SAR data.

Sangho An received the B.Sc. degree in atmospheric science from Pusan National University, Busan, South Korea, in 2020. He is currently working toward the M.Sc. degree in earth and environmental sciences with Seoul National University, Seoul, South Korea.

His research interests include radar signal processing and ground moving target indication.

Juyoung Song received the B.Sc. and M.Sc. degrees in earth and environmental sciences from Seoul National University, Seoul, South Korea, in 2019 and 2021, respectively, where he is currently working toward the Ph.D. degree in radar remote sensing and geophysics.

His research interests include vessel monitoring using synthetic aperture radar and radar signal processing.

Junwoo Kim received the B.Eng. degree in architecture from Yeungnam University, Gyeongbuk, South Korea, in 2011, the M.Sc. degree in remote sensing and GIS from Kyungpook National University, Daegu, South Korea, in 2014, and the Ph.D. degree in geography from the University of Leeds, Leeds, U.K., in 2019.

He was with the Institute of Basic Sciences at Seoul National University, Seoul, South Korea, between 2019 and 2020, as a Postdoc Researcher, and has been a Senior Researcher with the SNU Future Innovation Institute, Seoul National University, Seoul, South Korea, since 2020. His research interests include broadening and deepening our understanding of the earth and environments, and their interactions with human beings and society, using geospatial information technologies such as remote sensing, GIS, and artificial intelligence.